Chapter 15
Magnetic Antivortices

Matthias Pues and Guido Meier

Abstract We investigate the dynamics of magnetic antivortices by time-resolved magnetic X-ray microscopy and high-frequency absorption spectroscopy. A method for the reliable generation of isolated magnetic antivortices is devised using specifically formed microstructures and two-dimensional sequences of magnetic fields. For antivortices the measured resonance frequency is lower than for comparable vortices. The deflection of antivortices by external fields reveals strong deviations from a harmonic potential as well as rather low annihilation fields. Spectroscopy yields a characteristic absorption signal for antivortices for strong excitation that indicates a continuous switching of the antivortex core.

15.1 Introduction

Magnetic domains are regions with a homogeneous magnetisation. In soft magnetic materials like permalloy ($Ni_{80}Fe_{20}$) the magnetization in such domains lies in the film plane. A magnetisation pointing out of the plane would give rise to a large stray field and is prohibited by shape anisotropy. The coercive field of an extended film lies in the range of only a few mT. The in-plane magnetisation can be guided by the lateral confinement, as the shape anisotropy also tries to minimise the stray field on the sides, see Fig. 15.1. The energetically favoured state is a flux-closed magnetisation pattern, see Fig. 15.1c, d. The regions between the domains, the domain walls, can be separated into two main types: *Bloch walls* and *Néel walls*. In thin films, the

---

M. Pues
Institut für Angewandte Physik und Zentrum für Mikrostrukturforschung,
Jungiusstr. 11, 20355 Hamburg, Germany

G. Meier (✉)
Max-Planck Institute for the Structure and Dynamics of Matter,
Luruper Chaussee 149, 22761 Hamburg, Germany
e-mail: gmeier@mpsd.mpg.de

R. Wiesendanger (ed.), *Atomic- and Nanoscale Magnetism*, NanoScience and Technology, https://doi.org/10.1007/978-3-319-99558-8_15

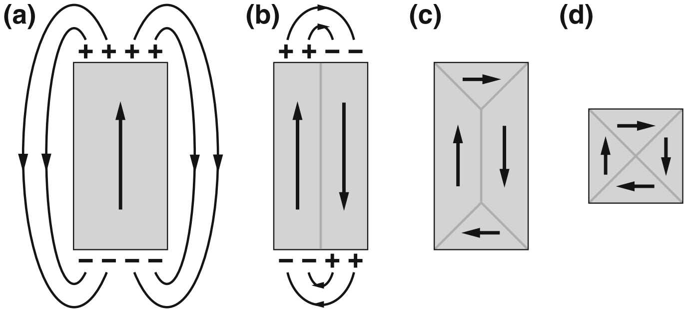

Fig. 15.1 Magnetic domains in in-plane magnetised thin film elements: **a** homogeneous magnetisation. **b** Two domains separated by a 180° domain wall. The stray field is reduced. **c** Triangular end domains close the inner flux. The so-called *Landau pattern* appears. **d** In equilateral polygons, like a square, the inner 180° domain wall becomes point-like

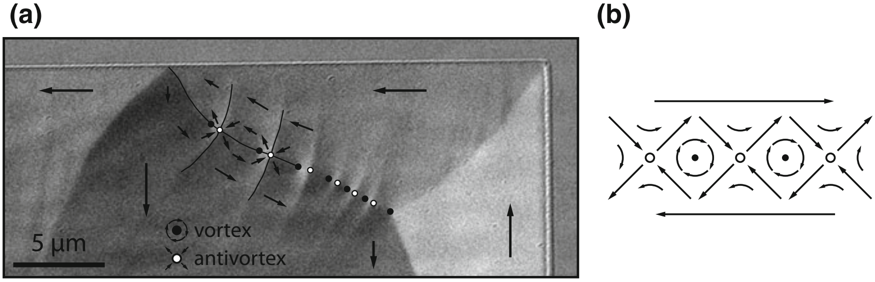

Fig. 15.2 Edge of a large permalloy rectangle observed by Kerr microscopy. The domains align along the edges of the microstructure. The chain of *vortices* and *antivortices* forming a *cross-tie wall* in the middle is partially marked. **b** Schematic of the magnetisation pattern of a 180° *cross-tie wall*

Bloch wall is characterised by a rotation of the magnetisation out of the plane of the substrate, whereas the rotation lies in the plane for Néel walls. For the investigated film thicknesses of up to 60 nm, Néel walls are the dominant type, but domain walls with a more complex inner structure also occur [1]. Figure 15.2a shows a larger permalloy rectangle, with an in-plane magnetisation, and a preferred orientation of the domains along the boundaries of the structure, as expected for this material. Some domain walls show no visible internal structure at this resolution, but the marked inner wall is a so-called *cross-tie wall*, a complex magnetisation pattern shown in Fig. 15.2b. This type of domain wall is a chain of special magnetisation points, where the opposing magnetic moments point antiparallel to each other. These magnetic quasi singularities are addressed as vortex and antivortex and are of special interest.

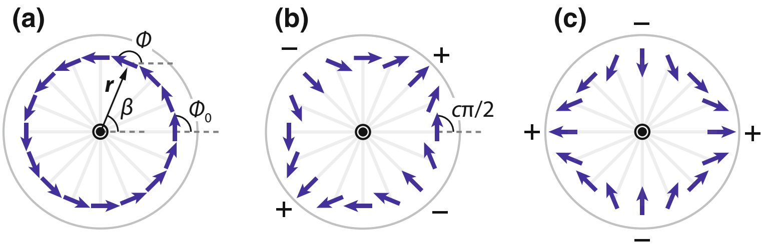

Fig. 15.3 Schematic magnetisation pattern of **a** a vortex with $c = +1$, and an antivortex with **b** $c = +1$ and **c** $c = 0$. The magnetic flux is not closed for the antivortex, indicated by the magnetic charges representing magnetic poles

15.2 Magnetic Singularities – Antivortices

The crossing points of the complex magnetisation pattern found in cross-tie walls are characterised by a specific winding of the magnetisation around the centre of those singularities [2]:

$$\phi(\beta) = n\beta + \phi_0 \quad \text{and} \quad \phi_0 = \frac{c\pi}{2}, \tag{15.1}$$

where ϕ is the angle of the local magnetisation vector with respect to the x-axis, β is the angle of the position vector $\boldsymbol{r}$ to the respective local magnetisation, see Fig. 15.3. The curling of the magnetisation is defined by the so-called winding number n, the orientation of the pattern by the offset angle ϕ_0. For $n = +1$, the magnetisation curls around the centre in a closed loop, see Fig. 15.3a, thus for $\phi = c\pi/2$ only two values are possible. The defining value $c = \pm 1$ is called circularity, as it determines the rotation direction of the magnetisation. For antivortices, with $n = -1$, the magnetisation curls in the opposite sense around the centre, see Fig. 15.3b. This pattern is not chiral, thus c can have any value in the interval $c \in [-2, 2[$ and is simply called the *c-value* or the orientation of the antivortex.

The antiparallel alignment of opposite moments in the centre of these magnetisation patterns is energetically unfavourable due to high exchange energy contributions for the large angles between neighbouring moments. This is overcome by a rotation out of the film plane of the centre magnetisation, see Fig. 15.4. The 180° angle is reduced to 90°. The orientation of the vortex or antivortex core up or down with respect to the z-axis is described by the polarisation p:

$$p = \operatorname{sgn} M_z(\boldsymbol{r} = 0) = \pm 1. \tag{15.2}$$

When considering the influence of external fields on both magnetic singularities, the quasi-static case and the dynamic case need to be discussed separately. In the quasi-static case, the change of the external field is slow compared to the intrinsic time scales of magnetization dynamics. Here, the domain pattern is shifted into the new

Fig. 15.4 Magnetisation pattern of the antivortex core. The inner region points out of the plane. A polarisation of $p = 1$ and orientation of $c = 1$ is shown

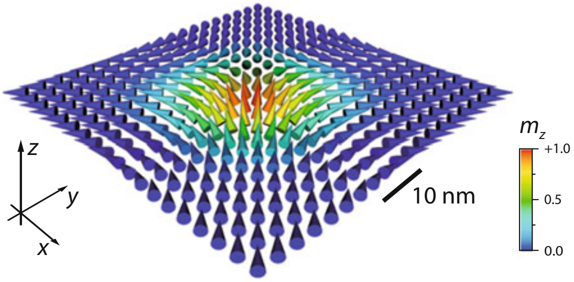

energetically favoured state according to the change in Zeeman energy induced by the external field. In a qualitative approach to estimate the new pattern, the domain with a magnetisation parallel to the applied field grows, while the one with an antiparallel magnetisation shrinks. For the dynamic case the Landau–Lifshitz–Gilbert equation (LLG) for the micromagnetic model can be used [3, 4]

$$\frac{d\boldsymbol{M}}{dt} = -\gamma \boldsymbol{M} \times \boldsymbol{H}_{\text{eff}} + \frac{\alpha}{M_{\text{s}}} \boldsymbol{M} \times \frac{d\boldsymbol{M}}{dt}, \tag{15.3}$$

where the effective field is the sum of the exchange field, the Zeeman field and the demagnetisation field

$$\boldsymbol{H}_{\text{eff}} = \boldsymbol{H}_{\text{ex}} + \boldsymbol{H}_{\text{Zeeman}} + \boldsymbol{H}_{\text{demag}}. \tag{15.4}$$

The gyromagnetic ratio in micromagnetism is defined as $\gamma = \mu_0 ge/2m_e$. M_S is the saturation magnetisation and α a phenomenological damping term introduced by Gilbert [3]. The first term of this differential equation describes the Larmor precession of the magnetic moment $\boldsymbol{M}$ around the effective field $\boldsymbol{H}_{\text{eff}}$. For the complex magnetisation pattern of a vortex or an antivortex the displacement of the equilibrium position by an external field yields a spiral-like motion [5]. This can be illustrated for the starting point of the core of the singularity, as the effective field is parallel to the applied field for this particular moment, see Fig. 15.5. For a vortex, the infinitesimal right hand rotation caused by the Larmor precession results in an effective core motion antiparallel to the effective field, see Fig. 15.5c. The antivortex however has a more complex structure, see Fig. 15.5b, d. Depending on the orientation, the situation is similar to the vortex as for the magnetisation of an intersection line along $c = \pm 1$. The magnetisation rotates to an axis parallel to the intersection, a so-called *Bloch-line* [6]. For an intersection at $c = 0$, the magnetisation rotates around an axis perpendicular to the intersection line, the Larmor precession yields a perpendicular displacement of the magnetisation pattern, i.e. the antivortex core, see Fig. 15.5d, f. A detailed analytical description of the vortex and antivortex dynamics can be found in [7].

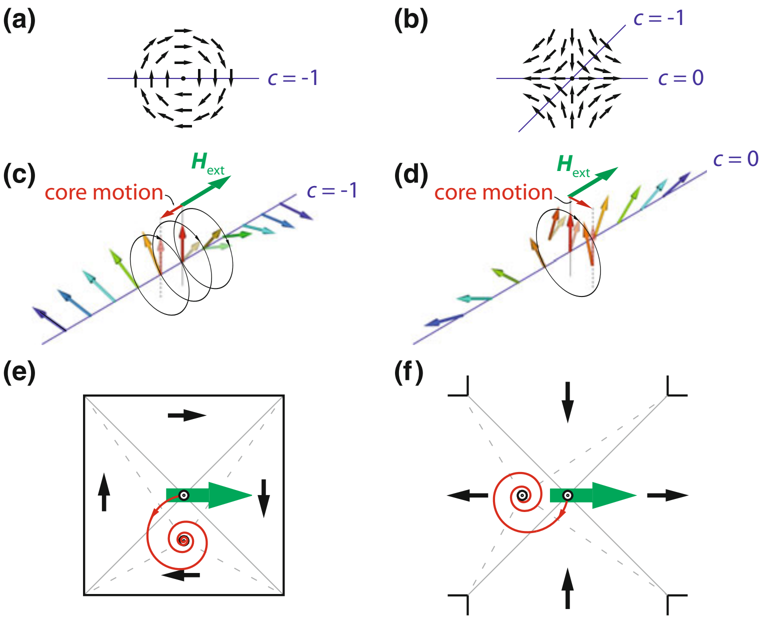

Fig. 15.5 Magnetisation pattern of **a** a vortex and **b** an antivortex with a polarisation $p = +1$. The magnetisation along certain intersection lines corresponds to **c** a *Bloch-line* for $c = \pm 1$ and **d** a *Néel-line* for $c = 0$. The Larmor precession induced by a magnetic field results in different effective core displacement directions. Gyrational motion of **e** a vortex core and **f** an antivortex core to the new equilibrium position caused by an external field

15.3 Antivortex Generation

The process of antivortex generation is understood by means of micromagnetic simulations and is experimentally demonstrated by X-ray transmission microscopy and magnetic force microscopy. The probability of antivortex nucleation is optimised by the variation of the structure geometry and the nucleation field strength. In contrast to the closed magnetisation of a vortex, which can be stabilised in thin-film structures with proper thickness and width that resemble a disc [8, 9], the in-plane magnetisation of an antivortex features four alternating poles, see Fig. 15.3b. The magnetic flux is not closed, but needs to be guided away from the centre region, thus the antivortex is metastable in a disc-like structure [10]. In the literature, different shapes have been shown to be suitable to stabilise antivortices [2, 11–14]. For micromagnetic simulations a star-like shape, whose contour is shaped by four adjacent discs, has been used [14], see Fig. 15.6a. The four apexes of the structure pin the magnetisation, pointing towards and away from the centre of the antivortex. The magnetic state can be predefined in the simulations, but to find the antiparallel alignment of the domains in real structures is very unlikely. Instead, in experiments this star-shape is used as a centre in a clover-shaped sample, see Fig. 15.6b, where wire loops close the magnetic flux

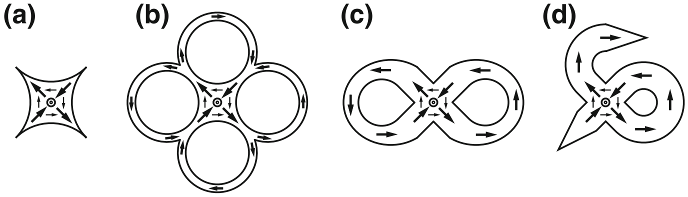

Fig. 15.6 Shapes of structures used to stabilise an antivortex: **a** star-like shape, **b** clover shape, **c** "infinity" structure, and **d** φ-shaped structure

[12]. After saturation of the magnetisation in such a sample, a successful regeneration of an antivortex with homogeneous external magnetic fields could not be observed. When altering the shape to a lemniscate, see Fig. 15.6c, the antivortex was found in some structures as the as-grown state. This so-called "infinity"-structure reduces the number of wire loops from four to two.

In principle the antivortex state could be recovered in such structures by a demagnetisation sequence of alternating fields of decreasing magnitude to annihilate possible multi-domain patterns that occur after the saturation [15]. Nonetheless the probability of the antivortex generation in these structures is too low to allow ensemble measurements. The reliable generation process proposed and demonstrated in this section makes use of a special shape of the structure and a two-dimensional bias field sequence to generate the antivortex. In addition, the field sequence is exactly specified and physically motivated so that it allows for high reproducibility and adaptability for other sample geometries. The φ-shaped design, see Fig. 15.6d, features three main characteristics that are crucial for the formation process: (i) tapered wire ends to pin the magnetisation along the wire and to prevent a magnetisation reversal after the saturation of the structure, (ii) curved segments to reproducibly create domain walls when saturated radially, and (iii) a wire junction in which the antivortex will be stabilised.[1]

The idea of the remagnetisation process is illustrated in Fig. 15.7a. The process starts with the saturation of the magnetisation in the φ-shaped structure in-plane with the saturation field H_s along the x-axis, see Fig. 15.7a step I. The coordinate system is defined by Fig. 15.7b. When the external field is lowered, the magnetisation aligns along the wires due to the now dominating shape anisotropy and two domain walls form in the curved segments, see Fig. 15.7a step II. This field amplitude is denoted as the nucleation field H_nuc. By a quasi-static counter-clockwise rotation of the in-plane field with a constant amplitude the domain walls are moved through the curved segments, see Fig. 15.7a II–IV. When both walls reach the wire junction, the antivortex nucleates, see Fig. 15.7a IV. The external field is then set to zero. The characterising parameters of such a remagnetisation, i.e. the saturation field H_s, the nucleation field H_nuc, and the nucleation field angle θ, cf. Fig. 15.7b, have to be

---

[1] Figures 15.6, 15.7, 15.9, 15.10, and 15.11 reprinted from M. Pues, M. Martens, T. Kamionka, and G. Meier, Applied Physics Letters **116**, 162404 (2012), with the permission of AIP Publishing.

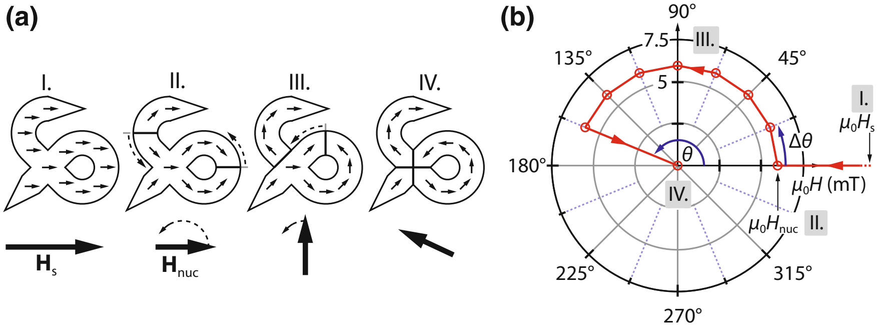

Fig. 15.7 **a** Schematic remagnetisation process of the φ-shaped structure: I. Saturation, II. domain-wall formation, III. domain-wall propagation driven by a quasi-static rotating magnetic field, IV. antivortex nucleation in the wire junction. **b** Polar graph of external in-plane fields used. An exemplary sequence of field steps for the remagnetisation process is shown

adjusted depending on the thickness, the wire width, and the edge roughness of each investigated structure.

The remagnetisation process is tested by means of micromagnetic simulations, as well as full field X-ray transmission microscopy performed at the Advanced Light Source (XM-1, beamline 6.1.2.) in Berkeley, CA, USA. In the simulation, the Gilbert damping is set to $\alpha = 0.5$. The high damping value is used as only the relaxed magnetisation states for the different bias fields are of interest, here. This and choosing a structure with a wire width of 0.5 mm, which is the size of the smallest experimentally analysed structures, reduces the computing time significantly. The height of the structure is 50 nm and the mesh cell size is $5 \times 5 \times 12.5$ nm^3. The simulation starts from a parametrised homogeneous magnetisation parallel to the x-axis and an external field of 80 mT in the same direction. Subsequently, the bias field is reduced to 20 mT in four steps and then in nine steps to the nucleation field $\mu_0 H_{\text{nuc}} = 8$ mT. The nucleation field is then rotated in steps of $\Delta\theta = 10°$. For the microscopy investigations, structures with two curved arms were used, see transmission X-ray micrographs in Fig. 15.8, for a more symmetric environment of the wire junction and to be able to investigate more domain walls within one microstructure. The elements have a wire width of 1 mm and a film thickness of 30 nm. To be able to achieve an in-plane contrast, the samples are tilted by 30° with respect to the X-ray beam path. The elements are tilted by $-22.5°$ in the plane with respect to the simulation in order to identify all four domains of the antivortex unequivocally when it is nucleated, cf. Fig. 15.8f, l. To depict the remagnetisation process the external field is set to the nucleation field strength after saturation at 100 mT in the x-direction and then rotated in-plane by steps of $\Delta\theta = 22.5°$. When decreasing the external field from saturation to the nucleation field, vortex domain walls form in the curved wire segments, see Fig. 15.8a, g. With the rotation of the external field, the domain walls move along the curved wire segments as expected. Different rotation angles are necessary in the simulation and the experimental microstructure, which can be explained by pinning

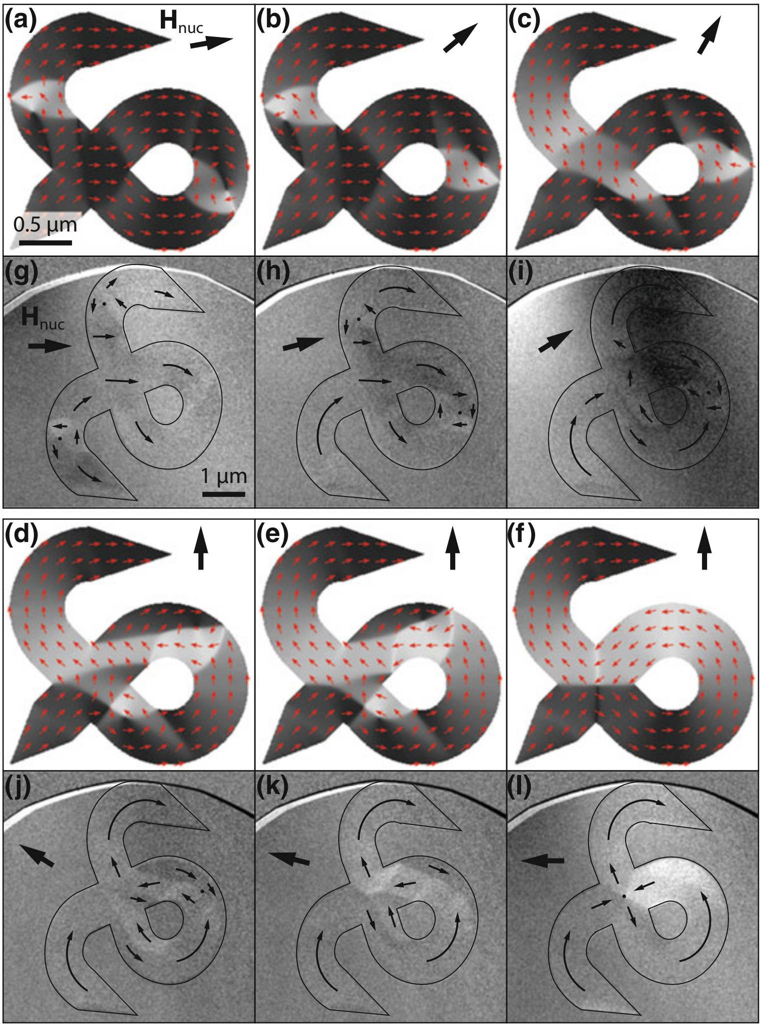

Fig. 15.8 Comparison of the simulated remagnetisation process (**a**)–(**f**) and transmission X-ray micrographs (**g**)–(**l**). Snapshots of the nucleation process for selected field angles are shown. The last images (f) and (**l**) show the stabilised antivortex. The nucleation fields are $\mu_0 H_{\text{nuc}} = 8$ and 3 mT, respectively. The greyscale represents the x magnetisation in both image sets. The element is tilted deliberately by −22.5° for the transmission microscopy samples to identify the antivortex unequivocally

of the domain walls at edge roughnesses on the wire walls and impurities within the wire. The vortex wall in the upper left arm moves into the junction, see Fig. 15.8c and (i), and forms an elongated 180° domain wall. From this wall, the antivortex nucleates, see Fig. 15.8d, and with the other vortex wall being pushed into the junction, the remaining vortices move towards the edges of the junction and annihilate.

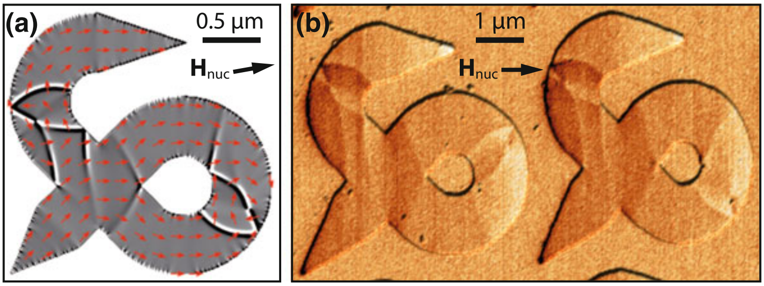

Fig. 15.9 Depiction of vortex domain walls in the curved wire segments by **a** micromagnetic simulation and **b** magnetic force microscopy. The greyscale in **a** represents the divergence of the magnetisation to be comparable with the MFM image. The nucleation fields are $\mu_0 H_{\text{nuc}} = 8$ mT and 5 mT, respectively

Finally in Fig. 15.8f, 1 the relaxed magnetisation constitutes an isolated antivortex that is stabilised in the wire junction.

The vortex walls can have either chiralities, showing no effect on the success of the remagnetisation process, which can be seen in the direct comparison of the simulated state and a magnetic force micrograph, see Fig. 15.9a, b. The magnetic force micrograph is recorded in an external field of 5 mT along the x-direction. Note that this and the following MFM images represent the first scan on that position after the saturation or remagnetisation. Thus the absence of characteristic lines in the micrographs due to a change of the magnetisation during the scan indicates a negligible influence of the magnetic tip on the magnetisation.

For a statistical analysis of the success of the remagnetisation process, arrays of identical structures were investigated with magnetic force microscopy. The array of structures in Fig. 15.10a are scanned after a remagnetisation with the parameters $\mu_0 H_s = 100\,\text{mT}$ and $\mu_0 H_{\text{nuc}} = 5\,\text{mT}$. The maximum rotation angle is $\theta = 135°$. The external magnetic field is generated with a pair of Helmholtz coils surrounding the microscope and a manual rotation of the sample. The micrograph shows that an antivortex could be generated in all 25 structures. Since the remagnetisation process determines the direction of the magnetisation in the wires of the junction, thus dictating the orientation or c-value [2] of the antivortex, a remagnetisation with a negative saturation and nucleation field leads to the opposite orientation of the generated antivortex. With the fixed orientation of the structure to the chosen coordinate system, a remagnetisation with positive field amplitudes leads to $c = -1$, see Fig. 15.10b, and with negative field amplitudes to $c = +1$, see Fig. 15.10c. If the wire width w of the structure is varied, different nucleation fields are required to ensure a successful antivortex generationx . Detailed MFM analyses like depicted in Fig. 15.10 of further arrays of 25 to 36 identical structures with wire widths from 0.5 to 1.4 µm reveal the expected influence of w and H_{nuc} on the probability of successful antivortex generation, see Fig. 15.10d, which can be understood as follows. With higher nucleation fields the probability increases because the field is then strong enough to overcome a pinning due to edge roughness and move the domain walls

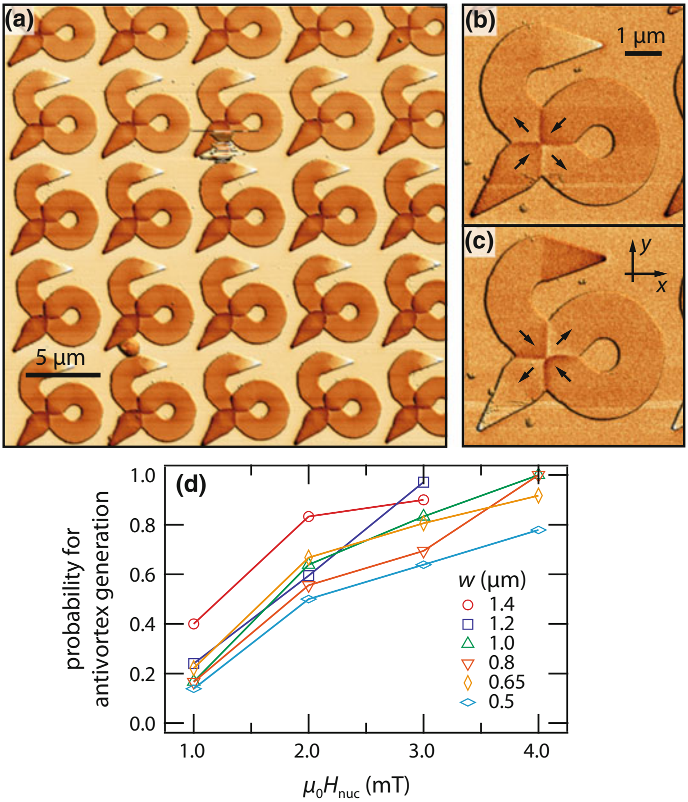

Fig. 15.10 **a** Magnetic force micrograph of an array of 25 φ-shaped structures after a remagnetisation process. All structures are in the antivortex state. Selected structures with antivortices of opposite orientations: **b** $c = -1$ and **c** $c = +1$. **d** Probability of a successful remagnetisation process for different nucleation fields and wire widths for an element height of 50 nm. Lines are guides to the eye

along the curved segments. The edge roughness is independent of w. Therefore, the ratio of the edge roughness to wire width becomes higher for smaller w. This results in a stronger pinning, explaining the higher fields necessary for successful antivortex generation for structures with smaller w. Note that the antivortex remagnetisation process is no longer successful for nucleation field strengths exceeding circa 10 mT, depending on the wire width.

The antivortex nucleation process has been investigated in detail showing how the manipulation of transient states of domain walls and vortices results in the desired antivortex state with a negative winding number of $n = -1$. The investigations reveal the reliability of the method for antivortex generation in φ-shaped structures with two-dimensional homogeneous in-plane fields. The antivortex-nucleation routine can now be used for spectroscopy, transport and X-ray microscopy measurements.

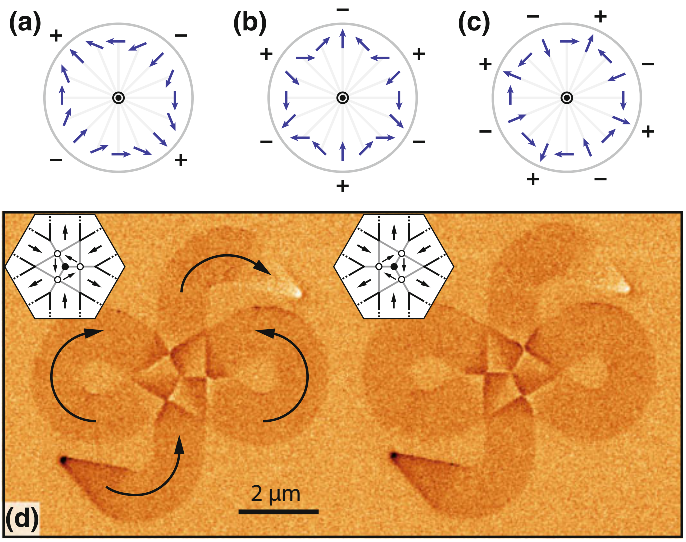

Fig. 15.11 Vector fields with winding numbers **a** $n = -1$, **b** $n = -2$, and **c** $n = -3$, all having an orientation of $c = -1$. **d** Magnetic force micrograph of two structures stabilising a magnetisation configuration in the junction with a total winding number of $n = -2$. The insets show the domain patterns within the junctions. Antivortices are indicated by circles, vortices by dots

15.4 Higher Winding Numbers

The method to control the magnetisation in curved nanowires with rotating in-plane fields can also be used to create even more complex domain patterns than antivortices. Magnetisation vector fields with decreasing winding numbers n exhibit increasing numbers of alternating magnetic poles around the centre, see Fig. 15.11a–c. Two structures designed so as to stabilise a hypothetical singularity with $n = -2$ are depicted in Fig. 15.11d. Before scanning the structures with a film thickness of 50 nm and a wire width of $w = 1.0\,\mu\text{m}$, they were remagnetised with a similar field sequence as the φ-structures with the parameters $\mu_0 H_\text{s} = 100\,\text{mT}$, $\mu_0 H_\text{nuc} = 5\,\text{mT}$, and $\theta = 360°$. The micrograph shows that the total winding number of the wire junction is in fact $n_\text{tot} = -2$. This is realised by the known stable singularities, by a vortex with $n = +1$, surrounded by three antivortices with $n = -1$. The chirality of the centered vortex is different in the two structures, resulting in a mirrored domain pattern, but not affecting the overall orientation.

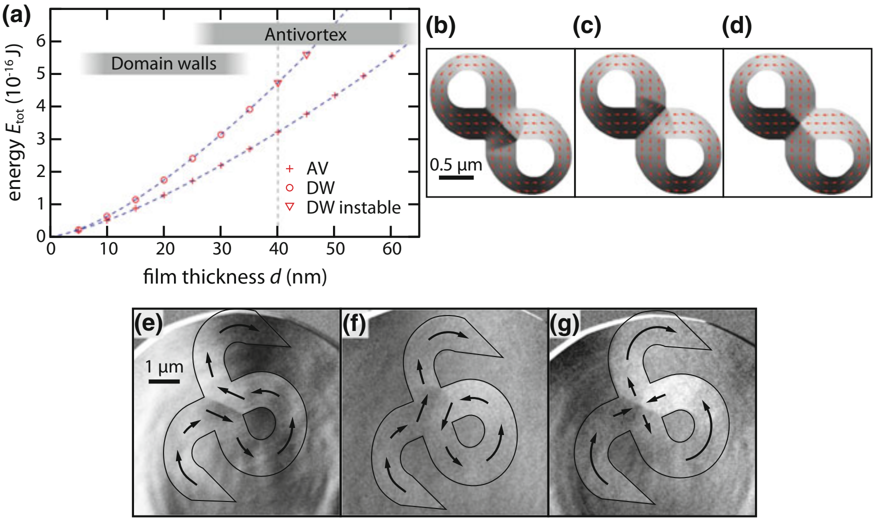

Fig. 15.12 **a** Total energy of antivortex or domain wall states obtained by micromagnetic simulations in infinity structures of different thickness. The two domain-wall states and the antivortex: **b**–**d** Simulated in a 50 nm thick infinity structure, and **e**–**g** measured by X-ray transmission microscopy in 30 nm thick symmetric φ-structures. Contrast shows the magnetisation in x-direction

15.5 Thickness Dependence

With the remagnetisation method discussed above an investigation of the thickness dependence of the antivortex and the opposing magnetic configuration, a 180° domain wall, is possible. A comparison of the total energy of the states obtained by micromagnetic simulations of infinity structures for film thicknesses of 5–60 nm shows that the domain wall can only be stabilised in elements with a thickness of up to 35 nm and transforms into an antivortex for a thicker element. The two domain wall configurations, see Fig. 15.12b, c, are nearly equal in energy, whereas the antivortex is always lower in energy, see Fig. 15.12a. As the simulations test only the static stability of predefined magnetic configurations, no direct conclusion can be drawn from the energy comparison to the probability of finding any of the different states in real elements, e.g. in the investigations by Bocklage et al. in [16], reporting an observation of a domain wall in a 20 nm thick infinity structure. Therefore, samples of symmetric φ-elements with thicknesses of 10, 20, 30, and 40 nm are investigated by full field transmission X-ray microscopy. The remagnetisation process is analysed for different nucleation fields, as well as the resulting magnetic states for the desired arm magnetisation. For the 10 and 20 nm samples only domain walls of both orientations can be observed, whereas for 30 nm, all three states occur, see Fig. 15.12e–g, cf. with (b)–(d). For 40 nm, only antivortices are generated by the remagnetisation sequence. This means that the domain wall is the dominant state for the used generation process for film heights up to 30 nm although it is higher in energy. Domain wall

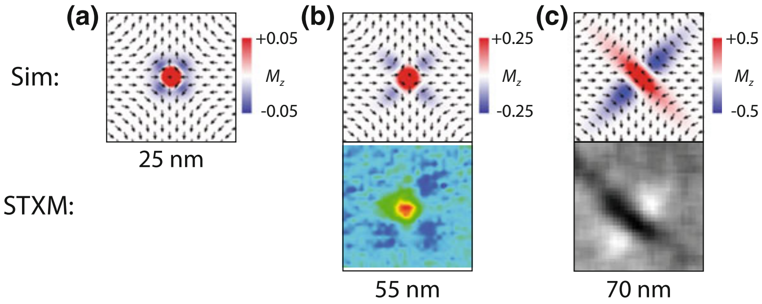

Fig. 15.13 Simulated antivortices for thicknesses **a** 25 nm, **b** 55 nm, and **c** 70 nm. Since the z-component is small for the thinner samples the colour scales are adjusted to 5, 25, and 50% M_z. The lower row shows scanning transmission X-ray micrographs of a 55 nm and a 70 nm thick structure at normal incidence

states cannot be found for thicker samples, as also indicated by the micromagnetic simulations, cf. shaded areas in Fig. 15.12a.

The upper thickness limit for antivortices is reached at 70 nm, where the four 90° domain walls from the kinks of the wire junction to the antivortex residing in the centre change from pure Néel walls to more complex walls. This can be seen in the change of the magnetisation pattern surrounding the antivortex core, simulated for different film heights, see Fig. 15.13. For thin films, the core is surrounded by a nearly circular region that points in an antiparallel direction to the core magnetisation out of the film plane. This ring divides into four distinguishable dips for 55 nm thick samples, as measured by scanning transmission X-ray microscopy at the MAXYMUS microscope of the BESSY II synchrotron in Berlin, Germany, see Fig. 15.13b. In direct proximity to the antivortex core, the 90° domain walls become Bloch like. For film heights above 65 nm the symmetry changes drastically, see Fig. 15.13c. The out-of-plane rotation of the domain walls becomes much more prominent and also two opposing domain walls change the sign of their z-magnetisation and fuse with the now parallel antivortex core. In this case the magnetic microstructure will no longer behave like a single 2D oscillator, as the antivortex or the vortex. No gyrational mode can be excited, but instead the antivortex performs a much more complex trajectory, since each domain wall itself is excited by the external fields. Moreover, the radius of the trajectory is decreased significantly. Consequently this analysis yields an optimal film thickness for isolated antivortices in permalloy from 40 to 60 nm.

15.6 Antivortices Influenced by Static and Dynamic External Magnetic Fields

With the method for antivortex generation proven to be reliable, the dynamics of isolated antivortices can be investigated spectroscopically by scalar network analysis. The influence of varying the exciting- and the static bias field on the gyrotropic

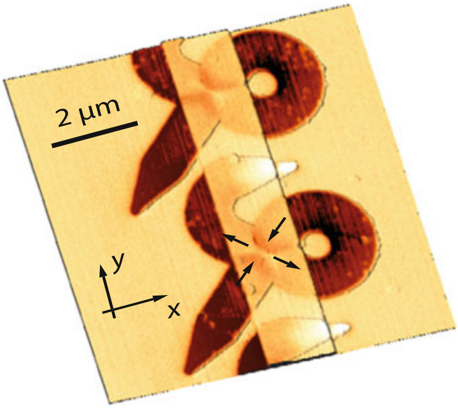

Fig. 15.14 Combined atomic and magnetic force micrograph of two φ-shaped permalloy microstructures overlaid by a copper stripline for high-frequency absorption measurements. The magnetic information shows an antivortex state in each structure

eigenmode of the antivortex is presented and discussed in the following. The spectroscopic measurements are complemented by magneto-resistance measurements and micromagnetic simulations [17].[2]

The resonance frequency of the gyrotropic eigenmode of isolated antivortices is determined by means of absorption spectroscopy. Figure 15.14 shows two φ structures of the ensemble, containing typically hundred antivortices, and the overlaying stripline, which generates the exciting Oersted field. A typical Lorentzian absorption spectrum for the antivortex ensemble is shown in Fig. 15.15b, with a resonance frequency of $f_{\text{res}} = 169\,\text{MHz}$. This frequency is approximately 40% lower than the resonance frequency of a vortex confined in a square-shaped element with the same film thickness and an edge length comparable to the wire width [20]. The lower frequency indicates a weaker confining potential if the antivortex is considered as a rigid quasiparticle as it is successfully done for vortices [21]. Absorption spectra for varying excitation power and thus for increasing Oersted field excitation are depicted in Fig. 15.15a. Three regions can be distinguished: (1) linear gyrotropic motion, (2) non-linear gyrotropic motion, and (3) continuous switching of the antivortex polarity. In regime (3) the cone-shaped absorption signal is caused by the continuous switching processes. For low excitation powers in regime (1), the resonance frequency is rather constant. The gyration of the antivortex can be described as a rigid quasiparticle in a nearly parabolic potential [19]. If the excitation power is increased, the resonance frequency drops significantly by about 20% in regime (2). In addition to the frequency drop, an asymmetric absorption curve can be observed in this nonlinear regime, see Fig. 15.15c. This asymmetry has also been reported for numerical simulations and measurements of resonance curves of vortices by Drews et al. in [18]. The core switching regime (3) is reached at $\mu_0 H_{\text{hf}} = 3\,\text{mT}$, indicated by the characteristic cone shaped signal [22] above 3 mT. The Oersted field to induce antivortex core switching is about six times the field strength needed to induce core switching

---

[2] Figures 15.15, 15.16, 15.18, 15.19, 15.20, 15.21, and 15.22 reprinted from M. Pues, M. Martens, and G. Meier, Journal of Applied Physics **116**, 153903 (2014), with the permission of AIP Publishing

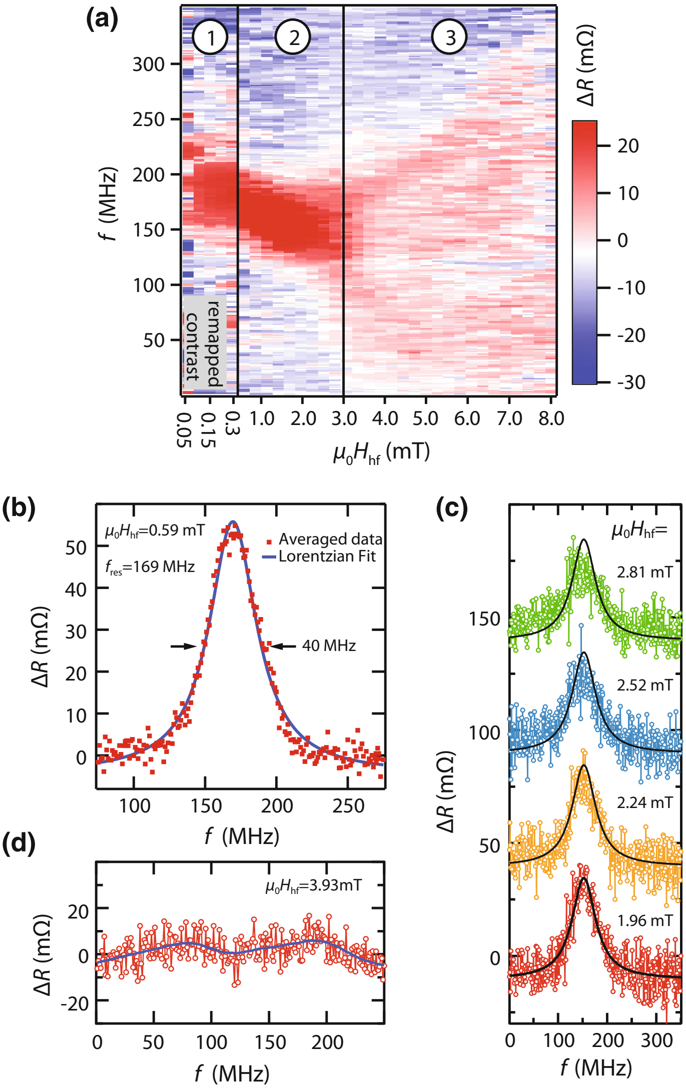

Fig. 15.15 Absorption spectra of antivortex generation. **a** Influence of the exciting field strength H_{hf}. The three regions are described below. **b** Frequency sweep in the linear regime. **c** Absorption signals for increasing excitation fields in the non-linear regime of the gyrotropic mode. The curves are offset successively by 50 mΩ. In order to show the increasing asymmetry and red shift of the absorption curves [18, 19], the same Lorentzian fit at the lowest excitation field strength of 1.96 mT is plotted as a solid line for all data curves. **d** Absorption signal from the core switching regime. The solid line is a guide to the eye

in a similar setup for vortices [20, 22]. The continuous switching of the polarity of the core is possible, since the linear excitation by the stripline can couple to both the clockwise and the counter-clockwise eigenmode of the antivortex. This is in contrast to the excitation by rotational Oersted fields [13] or rotational spin currents [15]. The absorption signal is reduced for strong excitation fields above 3 mT near the resonance frequency, which can be explained by the instability of the antivortex state, see Fig. 15.15d. If the antivortex switches its core polarisation multiple times at high-gyration radii, there is a probability that it moves away from the equilibrium position in the middle of the wire junction into one of the arms and is destroyed there. Since the absorption measurement is a time-integrating method, this process does not contribute to the ensemble signal. For vortices in discs, these considerations are irrelevant, since the vortex state is the energetically favoured state. Consequently, even if a vortex is destroyed, it will recover shortly after and will again contribute to the absorption signal.

15.7 Bias Field Dependence

To probe the confining potential of the antivortex, a static magnetic in-plane field is applied in eight different directions, $H_{\mathrm{ext}}(\Theta)$, in order to deflect the antivortex from the centre of the wire junction. Since the generation process of the antivortices determines the orientation of all antivortices in the ensemble, see Sect. 15.3, a single deflection direction of the whole ensemble can be ensured. An orientation of $c = -1$ is chosen for all measurements. A detailed description of the shift of the energy minimum due to this Zeeman field for vortices has been presented by Langner et al. in [23]. For the absorption spectroscopy a low excitation field in the harmonic regime of $\mu_0 H_{\mathrm{hf}} = 0.3\,\mathrm{mT}$ is chosen, see Fig. 15.16. The resonance frequency dependence of the static bias field $H_{\mathrm{ext}}(\Theta)$ shows a different behaviour for different field angles as well as a varying annihilation field $H_{\mathrm{an}}(\Theta)$ of the antivortices. At the annihilation field the antivortex is pushed out of the wire junction and consequently the absorption signal vanishes. Three types of frequency shifts can be distinguished. The frequency shift labelled (I) exhibits a small drop in the resonance frequency of 6 MHz, which corresponds to about 4%, as well as a decrease in the absorption. The annihilation field is around 2 mT. The second type (II) is characterised by a similarly small annihilation field, but shows a frequency increase of about 33 MHz (20%) with an increase of the absorption signal for bias field values close to the annihilation field. The third type (III) has relatively high annihilation fields of up to 8 mT and the resonance frequency rises about 25 MHz (15%). The small annihilation fields of antivortices in comparison to annihilation fields of vortices of about 35 mT [20] indicate again the comparably shallow potential, which confines the antivortex within the wire junction. Moreover, the anisotropy of the annihilation fields and the frequency shifts show a strong influence of the wire arms and the asymmetry of the confining structure on the antivortex.

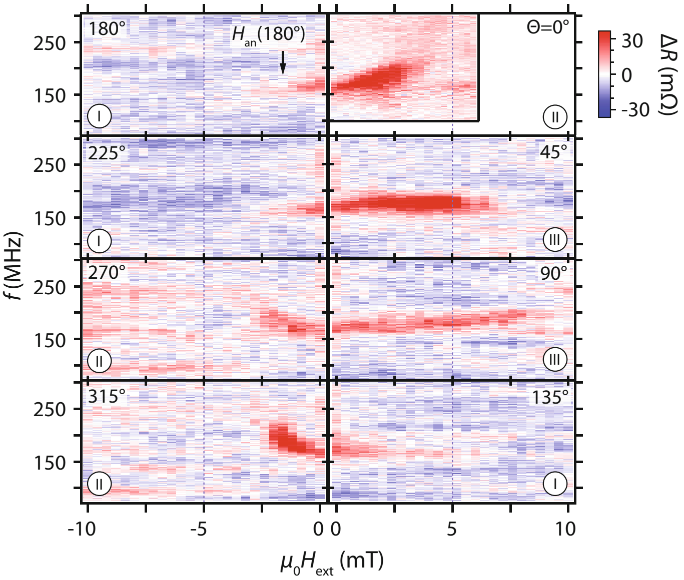

Fig. 15.16 Dependence of the antivortex resonance on a static bias field $H_{\text{ext}}(\Theta)$. The disappearance of the resonance signal for higher bias fields indicates the annihilation of the antivortex. The absorption spectra can be categorised into three types of frequency shifts (I, II, and III, compare Fig. 15.20)

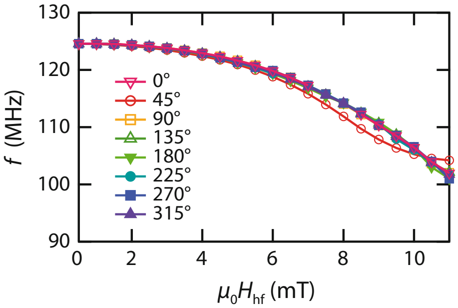

Fig. 15.17 Dependence of the free resonance frequency of the antivortex on a static in-plane bias field obtained by micromagnetic simulations. The frequency shift is nearly constant for every field angle, contrary to the experimental results. The change in frequency only deviates from the other curves for the field angle $\theta = 45°$ (red circles), when the antivortex is pushed into the straight arm

This complex resonance frequency dependence cannot be reproduced by micromagnetic simulations, cf. Figs. 15.16 and 15.17. To be able to achieve results for the eight different bias field angles within reasonable computation times, only the free gyration frequency is determined for the deflected antivortex. This may also give an explanation for the discrepancy to the experimental spectroscopy results. The

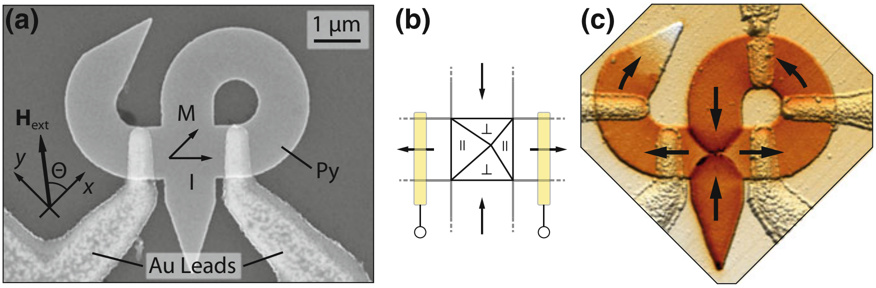

Fig. 15.18 **a** Scanning electron micrograph of a φ-shaped structure with Au contact leads for resistance measurements. **b** Scheme of a deflected antivortex. The triangularly shaped domains are denoted as parallel or perpendicular to the current flow. **c** Combined atomic and magnetic force micrograph of a contacted φ-structure containing an antivortex with an orientation of $c = -1$. For the MR measurements presented here, the structure with two contacts shown in **a** is used

simulations yield a uniform drop of the free gyration frequency for every bias field angle of about 23 MHz (18%). Only when pushed into the straight arm, the frequency shift differs slightly from the shifts caused by a bias field in the other directions, see Fig. 15.17.

To compare the drastic asymmetry of the annihilation field for gyrating antivortices with the annihilation fields for a static antivortex, magneto-resistance measurements are performed, see Fig. 15.19. The resistance of the wire junction of the φ-structure in saturation parallel to the current flow direction, indicated in Fig. 15.18a, is compared to the resistance after the antivortex generation and application of the bias in-plane field with angle Θ. This procedure is done for each data point, thus abrupt changes is the signal reveal the annihilation field of the antivortex for the corresponding bias field closest to zero fields in the MR signal. The following assumption leads to the identification of the antivortex state in the magneto-resistance signal: The magnetisation pattern of the antivortex consists of four triangularly shaped uniformly magnetised domains, see Fig. 15.18b, c. When a homogeneous current flows between the contact leads, a constant magnetisation within the wire arms, and no deformation of the 90° domain walls is assumed, the MR signal is expected to be constant to a good approximation for a deflected antivortex. Figure 15.19 shows this expected behaviour for the deflected antivortex state. The MR signal jumps from a nearly constant plateau to a MR signal indicating a magnetisation diagonal, perpendicular, or parallel to the current flow, see insets in Fig. 15.19. For some field angles the annihilation of the antivortex is followed by additional step-like transitions most likely due to sudden depinning processes of domain walls from the corners of the junction. As every data point represents a whole field sweep starting after an antivortex nucleation from zero field to either positive or negative field values, the smooth field dependence of the MR signal for each field angle indicates both a successful antivortex nucleation for every data point and a single path for the expulsion of the antivortex. The annihilation fields range from 7.2 to 12.7 mT and show a similar but much less distinct asymmetry compared to those derived from the absorption measurements, see Fig. 15.20a.

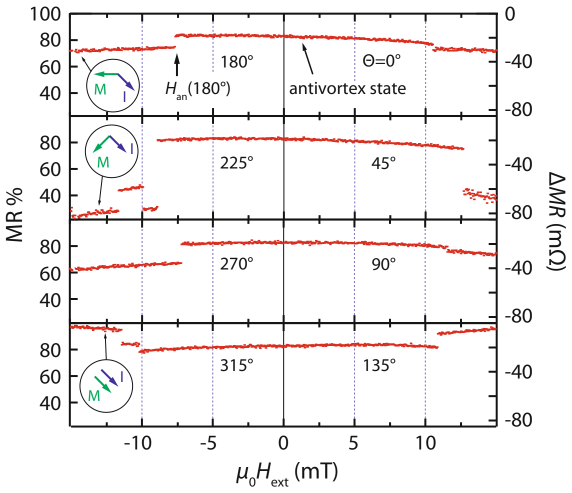

Fig. 15.19 Dependence of the magneto-resistance of an antivortex in the wire junction of a φ-shaped microstructure on a static bias field $H_{ext}(\Theta)$. The jumps in the signal indicate the annihilation of the antivortex

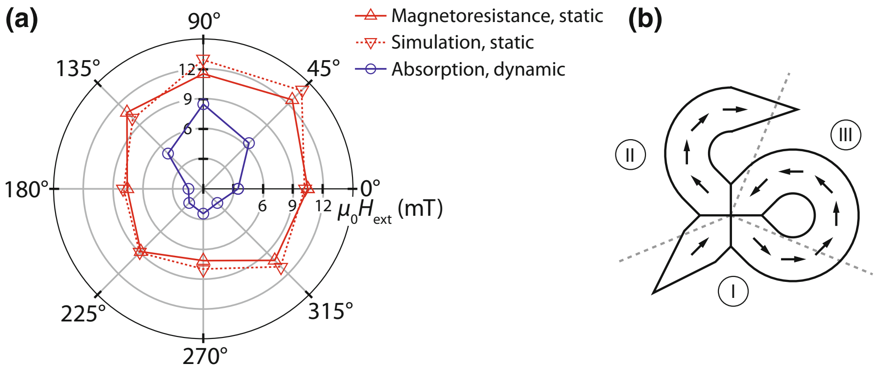

Fig. 15.20 **a** Comparison of the annihilation fields of the deflected antivortex for different in-plane field angles of the static field H_{ext}. Annihilation fields from magneto-resistance measurements, micromagnetic simulations, and high-frequency absorption measurements are shown. **b** Sketch of a φ-shaped structure. A deflection of the antivortex into one of the marked regions corresponds to the resonance frequency shift types from Fig. 15.16

15.8 Annihilation Process

Analogous to the MR measurements, micromagnetic simulations are performed, where the deflection of the antivortex by a quasi-static in-plane field $H_{ext}(\Theta)$ for eight different field angles as well as the free gyration frequency of the deflected antivortex is investigated. The simulated element is mapped from a scanning electron

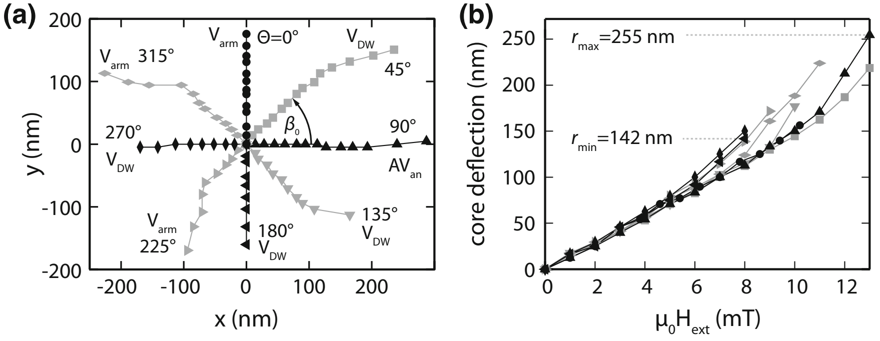

Fig. 15.21 **a** Simulated deflection from the equilibrium position of the core for bias fields with the indicated angle. The different annihilation processes (V_{arm}, V_{DW}, and AV_{an}) for each angle are explained in the text. **b** Distance from the equilibrium position at zero field of the antivortex core depending on the bias field obtained by micromagnetic simulations

micrograph of a real element, ensuring the same dimensions and edge roughness. The annihilation fields derived from these simulations match the ones determined by the MR measurements, see Fig. 15.20a. Furthermore, the simulations give a deep insight in the deflection behaviour of the antivortex, as well as in the annihilation process for different field directions. Figure 15.21b shows the core deflection distance from its equilibrium position for all fields with a minimal deflection of $r_{\mathrm{min}} = 142\,\mathrm{nm}$ and a maximal deflection of $r_{\mathrm{max}} = 255\,\mathrm{nm}$. A linear dependence of the core deflection on the external field with a slope of 14.6 nm/mT can be found up to about 5 mT, indicating the parabolic confining potential. For higher field strengths the slope increases up to the annihilation of the antivortex. This increase shows that the confining potential becomes shallower once the antivortex is pushed into the arms, which is contrary to the behaviour of isolated vortices. A vortex is confined in a closed microstructure like a disc or a square, resulting in a deviation from the parabolic confining potential near the boundary of the structure. Thus a vortex needs much stronger fields to be pushed towards the boundaries of the structure [18, 23, 24]. In the graph showing the core position for all field strengths and angles, see Fig. 15.21a, another effect of the open junction can be seen. For field strengths in the linear regime up to 5 mT, cf. Fig. 15.21b, the displacement of the core follows a fixed angle. This azimuth angle β_0 to the new equilibrium position of the core can be generally derived by $\beta_0 = n(\Theta + \pi - \Phi_0) = n(\Theta + \pi - c\pi/2)$, taking a rotational symmetric potential and the Zeeman energy into account. Here, the antivortex with a winding number [25] of $n = -1$ and the fixed orientation of $c = -1$ yields $\beta_0 = -\Theta - 3\pi/2$. At certain field strengths the core deflection deviates from this direction, mostly for the deflection into the arms. This can be attributed to the depinning of the 90° domain walls from the corners of the wire junction, see Fig. 15.22d, and a deformation of the walls. Moreover, for high field strengths the magnetisation within the arms, whose magnetisation points antiparallel to the external field, starts to bend in a zig-zag fashion, leading to the deflection of the core away from the centre of the arm. This

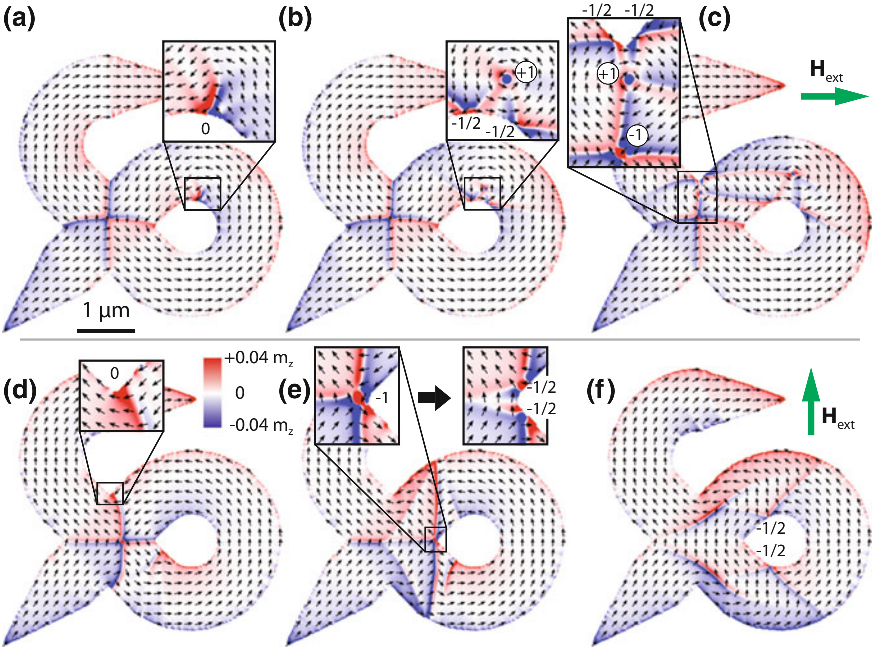

Fig. 15.22 **a**–**c** Sequence of the simulated annihilation process of the antivortex with an orientation of $c = -1$ by a static external field of $\mu_0 H_{\text{ext}} = 11\,\text{mT}$ in x-direction. **a** A 180° domain wall forms in a curved segment of the φ-shaped structure. **b** A vortex nucleates from the domain wall. **c** The upper 90° domain wall of the antivortex detaches from the corner of the wire junction forming another vortex. This vortex moves to the centre of the junction and both the vortex and the antivortex are annihilated. **d**–**f** Sequence of the annihilation of the antivortex at $\mu_0 H_{\text{ext}} = 14\,\text{mT}$ in y-direction. **d** The upper and lower 90° domain walls are no longer pinned at the respective corner and start moving into the arms. **e** The antivortex moves to the right corner and is annihilated there. Two edge defects are formed, that move further into the wire. The numbers denote the winding number of the respective magnetisation pattern

behaviour is not described by a simple rigid quasiparticle model of the antivortex, where the antivortex is confined in a parabolic potential. An extension of the parabolic potential to describe the deviation of the potential towards the boundaries of the structure has been done for vortices in squares [23], but for antivortices this approach poses several difficulties. For antivortices in φ-shaped structures the potential is highly anisotropic, whereas for vortices in squares only two different field directions have to be considered, i.e. towards the edge of the square and diagonally.

Similar shifts of the resonance frequency of the antivortex can be found for adjacent field angles and considering the deflection angle of the antivortex core caused by the external field reveals the influence of the φ-shaped structure on the confining potential, see Fig. 15.20b, even though the wire junction in which the antivortex is confined is completely rectangular. Thus a much more complex potential confines the antivortex.

An analysis of the antivortex annihilation for each field angle Θ reveals three different processes, as indicated in Fig. 15.21a. In Fig. 15.22 two of these annihilation processes are examplarily shown in the micromagnetic simulations for field angles of $\Theta = 0°$ in Fig. 15.22a–c, and 90° in (d)–(f). At an external field of $\mu_0 H_{\text{ext}}(0°) = 11\,\text{mT}$, the magnetisation in the upper right curved wire folds, forming a 180° domain wall, see Fig. 15.22a. From this wall a vortex nucleates and a domain that no longer points antiparallel to the external field is created, see Fig. 15.22b. This tilts the magnetisation in the upper right arm and destabilises the upper 90° domain wall of the antivortex. It detaches from the corner of the junction and another vortex nucleates from the former domain wall. The new vortex moves towards the antivortex and both are annihilated, see Fig. 15.22c. This process is labelled V_{arm} in Fig. 15.21a since the annihilation of the antivortex starts with the creation of a vortex in a wire arm. The second process, labelled V_{DW}, is similar, but a 90° domain wall of the antivortex detaches from the corner of the junction via a vortex nucleation without a preceding vortex nucleation in a curvature of the structure. The third process, AV_{an}, is only observed for a bias field in y-direction. The upper and lower domain walls of the antivortex depin from the corners, but are still attached to the boundary of the structure, see Fig. 15.22d. The domain walls and the antivortex start moving to the right until the antivortex core reaches the right corner of the wire junction, see Fig. 15.22e. Here the antivortex is annihilated and two edge defects [25] form, which move further along the inner boundary of the curved wire. Similarly, edge defects are generated when a vortex nucleates in the other processes described above. The magnetic texture of these edge defects can be described by half integer winding numbers $n = \pm 1/2$. When taking all magnetic defects that are generated or annihilated during the annihilation of the antivortex into account, it can be observed that the sum of the winding numbers of the whole structure remains $n_{\text{sum}} = -1$, the same as the initial antivortex. This holds for all bias field angles up to the maximum field strength of 15 mT in the simulation. The different annihilation processes exhibit no special symmetry that can be found in the φ-shaped structure, cf. Figs. 15.20b and 15.21a, but give a possible explanation of the anisotropy of the measured annihilation fields. For most cases, the antivortex is not pushed to the boundary of the wire junction and destroyed there, but its magnetic texture is distorted by changes of the magnetisation far from the antivortex. The annihilation processes for the real element may differ from the ones observed in the simulations, however a possible diversity in the annihilation mechanism is revealed. Thus it cannot be distinguished in the absorption and magneto-resistance measurements, if the annihilation field of the antivortex is measured or a field at which the magnetisation is reversed at some point in the φ-shaped structure by the external field as in the V_{arm} process.

The annihilation fields determined by MR measurements and micromagnetic simulations for a static antivortex are in good agreement, but the results from absorption spectroscopy, where the antivortex is gyrating at the resonance frequency, exhibit much smaller fields, see Fig. 15.20a. This discrepancy may not be attributed to high gyration radii and an expulsion of the antivortex from the decentred equilibrium position at a certain bias field. An estimation of the gyration radius r_{gyr} can be done by results from transmission X-ray microscopy on antivortices in elements with comparable dimensions [13, 15]. In these works maximal gyration radii of 95 to 115 nm at 140 and 120 MHz, respectively, are measured before core switching starts. Assuming a similar switching threshold for the structures presented here and a linear dependence of the gyration radius on the excitation field H_{hf}, the radius r_{gyr} can be estimated to be about 10 nm, a tenth of the maximal radius.

The displacement for the lowest annihilation field for the absorption measurements with $\mu_0 H_{\mathrm{an}}(180°) = 1.4\,\mathrm{mT}$ can be deduced from the simulations, where the constant deflection rate yields a displacement of the equilibrium position for this field of about 20 nm. The maximal displacement for a gyrating antivortex at this position can thus be estimated to be under 30 nm away from the centre of the wire junction, whereas it can be deflected up to 142 nm in the static case. Consequently, the reduced annihilation fields for the deflection of an excited antivortex cannot be attributed to the gyration radius of the antivortex, but rather to a reduction of the activation fields of the above described processes of domain wall depinning and vortex nucleation by the high-frequency field. A similar reduction of the switching field of a nanoparticle by radio-frequency field pulses is described by Thirion et al. in [26]. Thus the maximal gyration radius of about 100 nm before core switching starts, derived from the transmission X-ray microscopy results in [13, 15], and the minimal deflection distance of 142 nm for the static antivortex annihilation obtained by micromagnetic simulations (Fig. 15.21b) could explain the drastic decrease in the absorption signal for increasing excitation fields in the core switching regime, shown in Fig. 15.15a. It supports the above-mentioned hypothesis of an antivortex destruction for strong excitation fields and high gyration radii.[3]

Another comparison of the antivortex and the vortex can be made concerning the critical velocity needed for core switching. For vortices, a critical switching velocity $v_{\mathrm{crit}} = 2\pi r f_{res}$ was found by analytical and micromagnetic calculations [27] to be 320 m/s for vortices in discs or 250 m/s for vortices in squares by absorption measurements [22, 28]. The squares have comparable dimensions as the wire widths and thicknesses of the structures that stabilise the antivortex. The vortices in these squares exhibit a resonance frequency of 320 MHz and thus reach a gyration radius of about 124 nm at the critical velocity. The microscopy results for antivortices yield a much lower critical velocity of about 85 m/s at the comparable radii of 95 nm to 115 nm.

15.9 Conclusion

The gyrotropic eigenmode of isolated antivortices has been measured by high-frequency absorption spectroscopy for a varying excitation field strength in the linear, the non-linear and the core switching regime. The behaviour of isolated antivortices is similar to the one of excited vortices. When comparing antivortices with vortices

---

[3] In the transmission X-ray microscopy investigations in [13, 15] the disappearance of the antivortex core after several switching processes was occasionally observed.

of similar dimensions, the gyrotropic mode of the antivortex has a lower resonance frequency. To induce core switching, the antivortex needs to be exposed to a much stronger excitation field than the vortex. Deviations from a confining harmonic potential of the antivortex due to a static in-plane field have been demonstrated by the shift of the resonance frequency in the absorption measurements. To complement the anisotropy of the annihilation fields found in the absorption spectroscopy, magnetoresistance measurements as well as micromagnetic simulations have been discussed. While the annihilation fields determined from the MR measurements and the simulations without an excitation of the antivortex match quite well, the annihilation fields drop about 50% for the absorption spectroscopy, where the antivortex is excited. Moreover, a much more distinct anisotropy of the annihilation can be found for the excited state. It is demonstrated by means of micromagnetic simulations that for some field angles the annihilation of the antivortex is caused by a rotation of the magnetisation within an arm of the structure far away from the antivortex itself, thus destabilising the antivortex. These results show that a simple quasi-particle description for the antivortex is no longer applicable for the case of a strong excitation and an additional deflection of the equilibrium position by a static field.

Acknowledgements We are grateful to Ulrich Merkt for continuous support and fruitful discussions over many years. We thank Markus Weigand, Hermann Stoll, and Gisela Schütz, Max-Planck-Institute for Intelligent Systems, Stuttgart, Germany as well as Mi-Young Im and Peter Fischer, LBNL Berkeley, CA, USA for excellent, long-standing cooperation. We acknowledge financial support from the Deutsche Forschungsgemeinschaft via SFB 668 'Magnetism from the Single Atom to the Nanostructure', via Graduiertenkolleg 1286 'Functional Metal-Semiconductor Hybrid Systems', and via excellence cluster 'The Hamburg Centre for Ultrafast Imaging - Structure, Dynamics and Control of Matter on the Atomic Scale'.

References

1. S. Middelhoek, Domain walls in thin NiFe films. J. Appl. Phys. **34**, 1054 (1963)
2. A. Drews, B. Krüger, M. Bolte, G. Meier, Current- and field-driven magnetic antivortices. Phys. Rev. B **77**, 094413 (2008)
3. T.L. Gilbert, A Phenomenological Theory of Damping in Ferromagnetic Materials. IEEE Trans. Magn. **40**, 3443 (2004)
4. L. Landau, E. Lifshits, on the theory of the dispersion of magnetic permeability in ferromagnetic bodies. Phys. Zeitsch. der Sow. **169**, 14 (1935)
5. K.Y. Guslienko, B.A. Ivanov, V. Novosad, Y. Otani, H. Shima, K. Fukamichi, Eigenfrequencies of vortex state excitations in magnetic submicron-size disks. J. Appl. Phys. **91**, 8037 (2002)
6. J. Stöhr, H.C. Siegmann, *Magnetism: From Fundamentals to Nanoscale Dynamics* (Springer, Berlin, 2006)
7. M. Martens, T. Kamionka, A. Drews, B. Krüger, G. Meier, Influence of the winding number on field- and current driven dynamics of magnetic vortices and antivortices. J. Appl. Phys. **112**, 013917 (2012)
8. K.J. Kirk, S. McVitie, J.N. Chapman, C.D.W. Wilkinson, Imaging magnetic domain structure in sub-500 nm thin film elements. J. Appl. Phys. **89**, 7174 (2001)
9. T. Shinjo, Magnetic vortex core observation in circular dots of permalloy. Science **289**, 930 (2000)

10. A. Lyberatos, S. Komineas, N. Papanicolaou, Precessing vortices and antivortices in ferromagnetic elements. J. Appl. Phys. **109**, 023911 (2011)
11. A. Drews, B. Krüger, G. Meier, S. Bohlens, L. Bocklage, T. Matsuyama, M. Bolte, Current- and field-driven magnetic antivortices for nonvolatile data storage. Appl. Phys. Lett. **94**, 062504 (2009)
12. K. Shigeto, T. Okuno, K. Mibu, T. Shinjo, T. Ono, Magnetic force microscopy observation of antivortex core with perpendicular magnetization in patterned thin film of permalloy. Appl. Phys. Lett. **80**, 4190 (2002)
13. T. Kamionka, M. Martens, K.W. Chou, M. Curcic, A. Drews, G. Schütz, T. Tyliszczak, H. Stoll, B. Van Waeyenberge, G. Meier, Magnetic antivortex-core reversal by circular-rotational spin currents. Phys. Rev. Lett. **105**, 137204 (2010)
14. H. Wang, C. Campbell, Spin dynamics of a magnetic antivortex: micromagnetic simulations. Phys. Rev. B **76**, 220407 (2007)
15. T. Kamionka, M. Martens, K.W. Chou, A. Drews, T. Tyliszczak, H. Stoll, B. Van Waeyenberge, G. Meier, Magnetic antivortex-core reversal by rotating magnetic fields. Phys. Rev. B **83**, 224422 (2011)
16. L. Bocklage, B. Krüger, R. Eiselt, M. Bolte, P. Fischer, G. Meier, Time-resolved imaging of current-induced domain-wall oscillations. Phys. Rev. B **78**, 180405 (2008)
17. M. Pues, M. Martens, G. Meier, Absorption spectroscopy of isolated magnetic antivortices. J. Appl. Phys. **116**, 153903 (2014)
18. A. Drews, B. Krüger, G. Selke, T. Kamionka, A. Vogel, M. Martens, U. Merkt, D. Möller, G. Meier, Nonlinear magnetic vortex gyration. Phys. Rev. B **85**, 144417 (2012)
19. B. Krüger, A. Drews, M. Bolte, U. Merkt, D. Pfannkuche, G. Meier, Vortices and antivortices as harmonic oscillators. J. Appl. Phys. **103**, 07A501 (2008)
20. T. Kamionka, M. Martens, A. Drews, B. Krüger, O. Albrecht, G. Meier, Influence of temperature on the gyrotropic eigenmode of magnetic vortices. Phys. Rev. B **83**, 224424 (2011)
21. B. Krüger, A. Drews, M. Bolte, U. Merkt, D. Pfannkuche, G. Meier, Harmonic oscillator model for current- and field-driven magnetic vortices. Phys. Rev. B **76**, 224426 (2007)
22. M. Martens, T. Kamionka, M. Weigand, H. Stoll, T. Tyliszczak, G. Meier, Phase diagram for magnetic vortex core switching studied by ferromagnetic absorption spectroscopy and time-resolved transmission X-ray microscopy. Phys. Rev. B **87**, 054426 (2013)
23. H.H. Langner, T. Kamionka, M. Martens, M. Weigand, C.F. Adolff, U. Merkt, G. Meier, Vortex dynamics in nonparabolic potentials. Phys. Rev. B **85**, 174436 (2012)
24. J.-S. Kim, O. Boulle, S. Verstoep, L. Heyne, J. Rhensius, M. Kläui, L.J. Heyderman, F. Kronast, R. Mattheis, C. Ulysse, G. Faini, Currentinduced vortex dynamics and pinning potentials probed by homodyne detection. Phys. Rev. B **82**, 104427 (2010)
25. O. Tchernyshyov, G.-W. Chern, Fractional vortices and composite domain walls in flat nanomagnets. Phys. Rev. Lett. **95**, 197204 (2005)
26. C. Thirion, W. Wernsdorfer, D. Mailly, Switching of magnetization by nonlinear resonance studied in single nanoparticles. Nat. Mater. **2**, 524 (2003)
27. K. Guslienko, K.-S. Lee, S.-K. Kim, Dynamic origin of vortex core switching in soft magnetic nanodots. Phys. Rev. Lett. **100**, 027203 (2008)
28. A. Vansteenkiste, K.W. Chou, M. Weigand, M. Curcic, V. Sackmann, H. Stoll, T. Tyliszczak, G. Woltersdorf, C.H. Back, G. Schütz, B. Van Waeyenberge, X-ray imaging of the dynamic magnetic vortex core deformation. Nat. Phys. **5**, 332 (2009)